DOI: 10.13009/EUCASS2023-297
Aerospace Europe Conference 2023 – 10TH EUCASS – 9TH CEAS

Experimental analysis of the flow field over an aeroelastic flexible wind tunnel model for tail buffeting analysis

Julius Stegmüller⋆ †*, Andreas Molz*⋆*, Paloma García Guillén*⋆ *and Christian Breitsamter*⋆
⋆*Chair of Aerodynamics and Fluid Mechanics, Technical University of Munich*
Boltzmannstr. 15, 85748 Garching bei München, Germany
julius.stegmueller@tum.de
†Corresponding author

Abstract

Modern high-agility aircraft are often affected by the consequences of tail buffeting effects at medium to high angles of attack. High pressure fluctuations with distinct frequency contents characterize the flow field downstream of the vortex breakdown and are responsible for the dynamic structural response. For analyzing the flow field and the frequency content of the pressure fluctuations over a modular full-span wind tunnel model with either rigid or flexible double-delta wings and horizontal and vertical tailplanes, stereoscopic particle image velocimetry measurements and measurements with a fast-response aerodynamic pressure probe are performed. When comparing the rigid and flexible configurations, significant differences in the axial vortex core velocities in some measurement planes can be detected, while the power spectral densities of the pressure fluctuations show similar characteristics with slight differences in the amplitudes.

1. Introduction

Tail buffeting effects often occur in modern high-agility aircraft, especially at low to high subsonic Mach numbers and medium to high angles of attack (AoA). Low aspect-ratio wings and medium to high sweep angles characterize these configurations. Even at low AoA, the boundary layer around the leading edge rolls up with the entrained flow and forms a large-scale leading-edge vortex. High axial velocities in the vortex core, low static pressure, and lower total pressure due to high dissipation in the sub-core characterize these leading-edge vortices [1]. With increasing AoA, the core flow becomes unstable, indicated by the rapid change in the axial velocity profiles and an adverse axial pressure gradient over the wing [2]. Above a certain AoA, the vortices burst, and the breakdown location moves upstream with further increase of the AoA [1]. The flow field downstream of vortex breakdown is characterized by high turbulent intensities and distinct frequency contents [1]. The spectra may show narrow-frequency band peaked distributions, leading to an enormously increasing buffet excitation level above a specific AoA [2]. The structural response to the aerodynamic excitation by the unsteady flow field is known as buffeting [3]. Thereby, the aerodynamic excitation is coupled with the structural response comprising the interaction of unsteady aerodynamic forces, inertia forces, and elastic forces. The unsteady aerodynamic forces relate to local flow separation and lifting surface motions (vibrations). Wing and tailplanes of modern high-agility aircraft are often affected by buffeting, which can lead to degraded handling qualities and to a reduction of the lifespan of structural components.

John [4] critically reviewed the feasibility of the available theoretical and experimental measures to quantify buffeting loads on aeroelastic aircraft structures and concluded that wind tunnel experiments with scaled flexible models are most favorable to predict buffet responses accurately. Rainey and Igoe [5] pointed out in their experimental wing and tail buffeting studies that transferring buffet loads quantitatively from the model to the aircraft is justified only when structural dynamic scaling is used. For scaling an aeroelastic model, the quantities dimensions, mass, moments of inertia, stiffness, and natural frequencies must be considered [6]. Davis Jr. and Huston [7] emphasize the problem of sting mounting the model, which could cause additional modes to be measured due to the rigid-body vibrations of the flexible sting support. Investigations regarding structural dynamic scaling on aeroelastic wind tunnel models and the transfer of determined structural parameters to full-scale design have been carried out by Hanson [8], John [4], and Zan and Huang [9], among others. For analyzing tail buffeting effects, a flexible wind tunnel model using rapid prototyping material was developed in cooperation between Airbus Defence and Space and the Chair of Aerodynamics and Fluid Mechanics at the Technical University of Munich [10]. The flexible components 3D-printed from polylactide (PLA) are scaled with respect to a possible generic large-scale configuration considering structural elasticity. Quasi-rigid lifting

DOI: 10.13009/EUCASS2023-297

surfaces made of aluminum are used as a comparative configuration. The aerodynamic excitation was measured with piezo-resistive pressure transducers, the structural dynamic response with miniature accelerometers and strain gauges [11]. Based on the experience gained with an aeroelastic half model, an aeroelastic full-span model with 76°/40° double-delta wings, horizontal stabilizers, and fins was developed and aeroelastically analyzed with transient pressure transducers and accelerometers [12]. The 76°/40° double-delta wing planform has been extensively investigated in the scientific community, e.g., by Verhaagen et al. [13], Cunningham Jr. et al. [14], Gonzalez et al. [15] and Woodiga et al. [16]. Brennenstuhl and Hummel [17] investigated the influence of the leading edge sweep of the outboard wing section and the axial kink position on the vortex characteristics of double delta wings.

For analyzing the flow field experimentally with its burst vortices, which, acting as aerodynamic excitation, are responsible for the structural response or buffeting, stereoscopic particle image velocimetry (Stereo-PIV) measurements can be used. Taylor and Gursul [18] performed PIV water tunnel measurements for vortex flow visualization over a non slender delta wing with a 50° leading edge sweep angle. Pfnür and Breitsamter [19] investigated the overall flow field and vortex system of a double- and a triple-delta wing at low subsonic flow with Stereo-PIV including breakdown locations, vortex core data, vortex trajectories, and the flow patterns of the vortex system. Sedlacek and Breitsamter [20] analyzed the vortex development, interaction, and breakdown at sideslip conditions of a double- and a triple-delta wing at low subsonic flow conditions. For a triple-delta wing, Sedlacek et al. [21] analyzed the flow field pattern based on Stereo-PIV data and the spectral characteristics of the velocity field fluctuations using a fast-response aerodynamic pressure probe (FRAP).

Several Stereo-PIV studies analyze vortical flows over highly swept wings with downstream located objects like fins. Woppowa and Grosche [22] carried out water tunnel PIV measurements with variable sweep angles of the wing ($\varphi_W = 25°$ and $\varphi_W = 68°$) to analyze the instantaneous flow field and vorticity distribution for a low sweep and high sweep high-agility aircraft configuration. Wolfe et al. [23] and Mayori and Rockwell [24] investigated experimentally in a water tunnel the interaction of the vortex breakdown with a thin plate downstream of a delta wing. Canbazoglu et al. [25, 26] used a swept fin in combination with a 75° swept delta wing to characterize the interaction between a burst vortex and a fin with PIV in a water tunnel. For extracting the most energetic flow structures of vortex-tail interaction, Kim and Rockwell [27] applied a proper orthogonal decomposition (POD) to PIV measurements with a 75° swept delta wing combined with a swept tail also in water tunnel.

In the present study, the focus of flow field analysis by Stereo-PIV measurements is on the comparison of a flexible configuration with a quasi-rigid reference configuration, which to the best of the authors' knowledge is a novel investigation. For the wind tunnel studies, the aeroelastic full-span model with 76°/40° double-delta wings, horizontal stabilizers, and fins (see Stegmüller et al. [12]) is used. Selected cross-flow sections are analyzed transiently using a FRAP.

The present paper is structured as follows. Section 2 describes the experimental setup with the design of the wind tunnel model, the Stereo-PIV measurement setup, and the FRAP measurement setup as well as the measurement conditions. In section 3, the results of the wind tunnel experiments are analyzed and discussed with a focus on the comparison of the rigid with the flexible configuration. After describing the flow field over the wind tunnel model for $\alpha = 25°$ and $\alpha = 35°$, the vortex trajectories and axial core velocities are discussed. Subsequently, the flow field in the breakdown areas is analyzed, using two Stereo-PIV planes per AoA. Finally, the flow field for $\alpha = 25°$ is analyzed for the spectral content in the pressure fluctuations, using the FRAP measurements. Section 4 summarizes the results and gives an outlook.

2. Experimental setup

2.1 Design of the wind tunnel model

An aeroelastic full-span model was developed in [12] to study buffeting effects experimentally. The design concept is centered around two key ideas. Firstly, a quasi-rigid configuration allows for a detailed flow-physical analysis of the vortex systems and the aerodynamic excitation they produce. Secondly, a configuration with flexible lifting surfaces enables the investigation of the aeroelastic structural response. Hence, the modularity of the wind tunnel model design holds significant importance. Both the rigid and the flexible lifting surfaces can be attached to the rigid aluminum fuselage. The rigid components are made of aluminum, while the flexible components are 3D-printed from PLA. The flexible components are scaled with respect to a possible generic large-scale configuration considering structural elasticity, i.e., especially wing, horizontal tail plane (HTP), and fin deformation, and structural dynamics regarding wing, HTP, and fin bending and torsion modes, cf. similarity rules [28, 29, 6]. The HTPs are mounted to the fuselage in a way that allows for different deflection angles. In contrast to the quasi-rigid HTP, which is manufactured as a single unit, the flexible HTP is connected to an aluminum connector. This also enables a robust clamping connection with the rear fuselage cover for the flexible HTP. The investigations of this study are carried out without an angular deflection

DOI: 10.13009/EUCASS2023-297

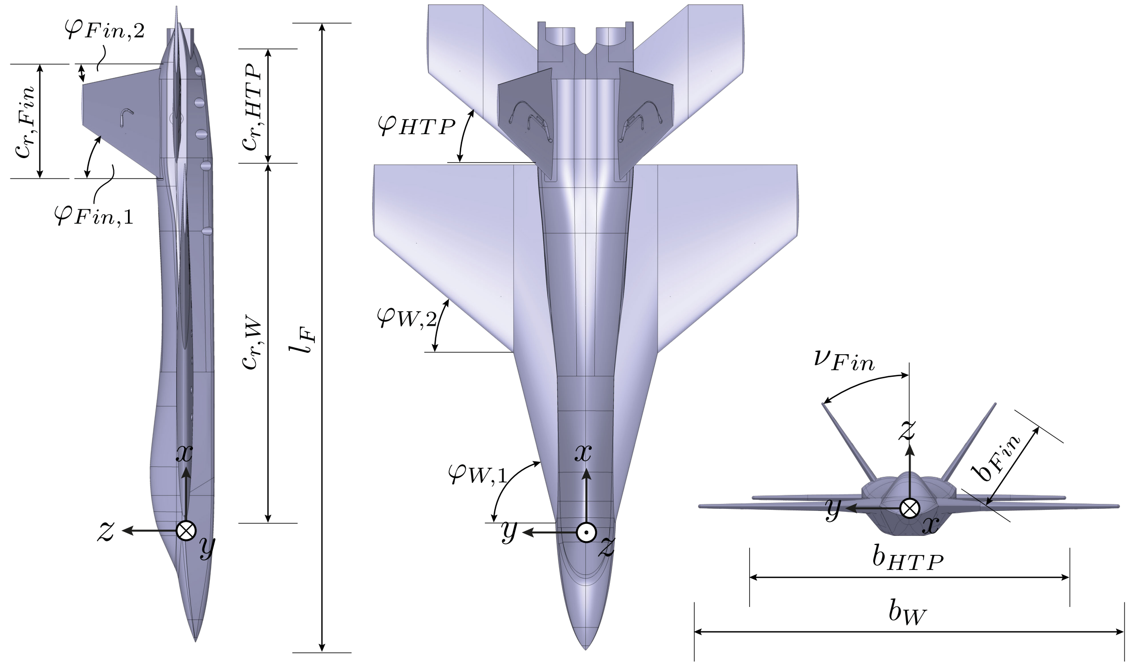

Figure 1: Basic parameters of the wind tunnel model [12]

of the HTP ($\delta_{HTP} = 0°$).
The wing, HTP, and vertical fin are all based on the NACA 64A-005 airfoil type. Figure 1 provides multiple perspectives of the model and presents the fundamental parameters. The specific parameter values can be found in Table 1. Similar to the half model developed by Katzenmeier et al. [10], the full-span model features a double delta wing design with a sweep angle of $\varphi_{W,1} = 76°$ at the strake and $\varphi_{W,1} = 40°$ at the outboard wing section. The leading and trailing edges of the HTP have a sweep angle of $\varphi_{HTP} = 40°$. The fins are deflected by $\nu_{Fin} = 34°$ relative to the xz-plane. The leading edge of the fins exhibits a sweep angle of $\varphi_{Fin,1} = 30°$, while the trailing edge has a sweep angle of $\varphi_{Fin,2} = -10°$. With a fuselage length of $l_F = 1.1$ m, the model possesses a wing root length of $c_{r,W} = 0.66$ m and a wingspan of $b_W = 0.74$ m. The mean aerodynamic chord measures $l_\mu = 0.427$ m, and the wing reference area is $S_{ref} = 0.25\,\text{m}^2$. The HTP's and fin's root length is $c_{r,HTP} = c_{r,Fin} = 0.2$ m. The HTP has a span of $b_{HTP} = 0.55$ m, and the fin's length or span is $b_{Fin} = 0.17$ m, as depicted in Fig. 1. Additionally, the HTP features a vertical offset by 0.015 m in the positive z-direction relative to the wing plane, deliberately inducing higher vortex-induced turbulence intensity and pressure fluctuations at the HTP. More information regarding the model setup with integrated sensors and first measurement results (force and moment polar, transient surface pressures, and vertical tip accelerations) can be taken from Ref. [12].

Table 1: Parameter values of the wind tunnel model [12]

Wing/Fuselage		**HTP/Fin**	
l_F	1.1 m	$c_{r,HTP} = c_{r,Fin}$	0.2 m
l_μ	0.427 m	$c_{r,HTP}/c_{r,W}$	0.3
$c_{r,W}$	0.66 m	b_{HTP}	0.55 m
b_W	0.74 m	b_{Fin}	0.17 m
$\varphi_{W,1}/\varphi_{W,2}$	76°/40°	$\varphi_{HTP}/\varphi_{Fin,1}/\varphi_{Fin,2}$	40°/30°/ − 10°
S_{ref}	0.25 m^2	ν_{Fin}	34°

2.2 Stereo-PIV measurement setup

The flow field in multiple cross-sections is examined using a Stereo-PIV measurement system. Figure 2 shows the measurement setup on the left-hand side. The Stereo-PIV system is mounted on a three-axis traversing system next to the wind tunnel test section. The traversing system can be rotated around the lateral axis to ensure that the camera

DOI: 10.13009/EUCASS2023-297

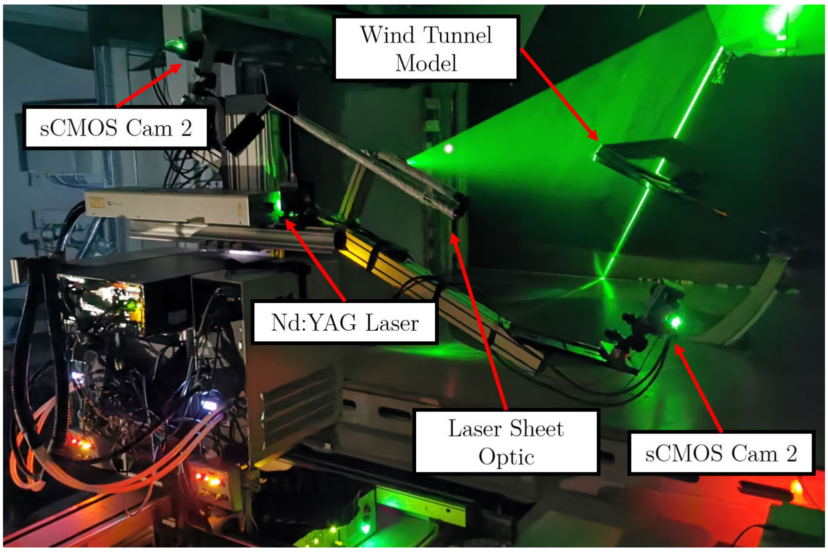

(a) Stereo-PIV measurement setup

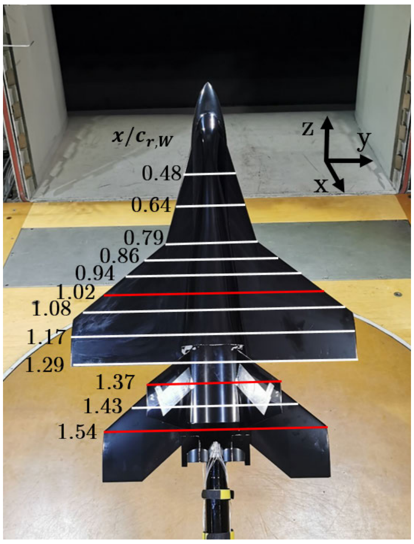

(b) Sting mounted wind tunnel model

Figure 2: Stereo-PIV measurement setup and wind tunnel model integrated into the test section

frames and the laser sheet are perpendicular to the wing surface for every AoA of the wind tunnel model. The measurement plane is illuminated by a double-pulsed neodymium-doped yttrium aluminum garnet (Nd:YAG) laser. The laser features maximum power of 325 mJ per pulse and a wavelength of 532 nm. Two scientific complementary metal oxide semiconductor (sCMOS) cameras with a resolution of 2560 × 2160 pixels are placed up- and downstream of the measurement plane with an angle of 60°. Each camera has a Scheimpflug adapter to tilt the sCMOS sensor plane and fulfill the Scheimpflug criterion (see Hinsch [30]). Table 2 summarizes the most important information about the Stereo-PIV setup and the parameters of the vector calculation. The measurement plane measures 0.45 m × 0.21 m. The sampling frequency for 400 image pairs per measured cross-flow section is 15 Hz. Di-Ethyl-Hexyl-Sebacate (DEHS) particles act as the seeding for the measurements and have a diameter of ≈ 1 µm. The described measurement setup enables a spatial resolution of $\Delta d = 1.49 \times 10^{-3}$ m and a nondimensional spatial resolution with respect to the wing half span of $\Delta d/s = 4.03 \times 10^{-3}$ m. The uncertainties of the mean velocity components were quantified to $|u_{err}/U_\infty| < 0.06$ and $|v_{err}/U_\infty| = |w_{err}/U_\infty| < 0.035$ [31].
A total of 12 planes were measured at an AoA of $\alpha = 25°$ and 11 planes at $\alpha = 35°$. Due to the limitation of the traversing system, the first plane near the apex of the wing could not be measured at $\alpha = 35°$. The right-hand side in Fig. 2 shows the wind tunnel model mounted on the sting in the test section of the wind tunnel with the position of the measured planes. The red planes mark the flow cross-sections measured with the FRAP. The non-dimensional x-position of the planes $x/c_{r,W}$ is referred to the nose of the fuselage.

Table 2: Stereo-PIV setup and processing parameters

Parameter	Value
Angles between cameras [°]	60
Diameter of the seeding particles [μm]	≈ 1
Number of samples [-]	400
Sampling frequency [Hz]	15
Measurement field dimension [m^2]	$d_y \times d_z \approx 0.45 \times 0.21$
Spatial resolution [m]	$\Delta d = 1.49 \times 10^{-3}$
Non-dimensional spatial resolution [-]	$\Delta d/s = 4.03 \times 10^{-3}$

2.3 FRAP measurement setup

To investigate the flow field over the double-delta wing configuration with HTPs and fins for time accurate characteristics and in terms of power spectral densities (PSD), selected cross-flow sections (marked red in Fig.2b) were measured

DOI: 10.13009/EUCASS2023-297

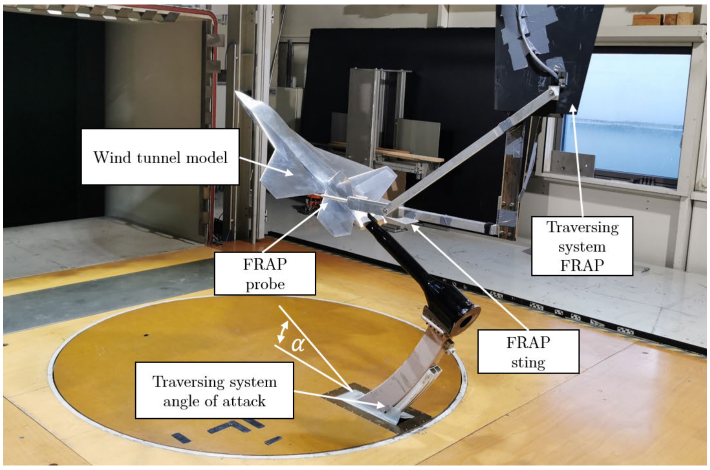

(a) Wind tunnel model and FRAP each mounted on their traversing system

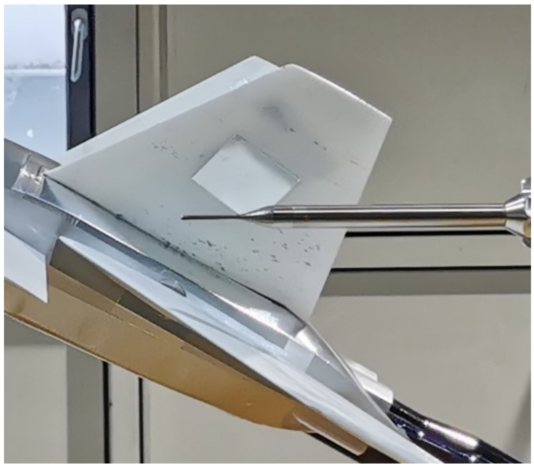

(b) Close-up of the FRAP

Figure 3: Setup of the FRAP measurements

with the FRAP. For measuring the velocities within a cone angle of 60°, five piezo-resistive differential pressure sensors (Meggitt Endevco 8507c-2) with a pressure range of 2 psig are placed inside the probe shaft [32]. The tip diameter of the probe measures 3 mm. By considering calibration data from both temporal and spatial calibrations, the post-processed measured pressures enable a high level of reconstruction accuracy, achieving an angular deviation below 0.2° in both flow angles and a maximum deviation of 0.1 m/s in the reconstructed velocity, as demonstrated in the study by Heckmeier and Breitsamter [33]. In addition to spatial calibration for many velocity-angle combinations, the probe is temporally calibrated to compensate for acoustic pressure distortions such as resonance and attenuation [34]. Figure 3 shows the wind tunnel model mounted on a traversing system to adjust the AoA α and the FRAP with its traversing system to measure a complete grid automatically on the left-hand side. On the right-hand side, there is a close-up of the FRAP. Figure 4 visualizes the measurement setup. For the five pressure sensors of the FRAP, two NI 9237 data acquisition cards are required. The NI cDAQ-9185 chassis synchronizes the measurements of all sensors and transfers the data to the LabView-controlled computer. The FRAP can be moved three-dimensionally in space via a corresponding traversing system above the test section, which is also connected via a controller to the computer to automate the measuring task. While the measurement planes are always perpendicular to the longitudinal axis of the model in the yz-plane of the body-fixed coordinate system, the FRAP itself is always oriented against the freestream direction in the aerodynamic coordinate system. The wind speed is measured with a Prandtl probe in the freestream of the nozzle outlet. The measuring time per measuring point is 10 s at a sampling rate of $f_s = 10$ kHz. To avoid aliasing, a lowpass filter, which is automatically included in the data acquisition cards, is applied at $0.45 \times f_s$.

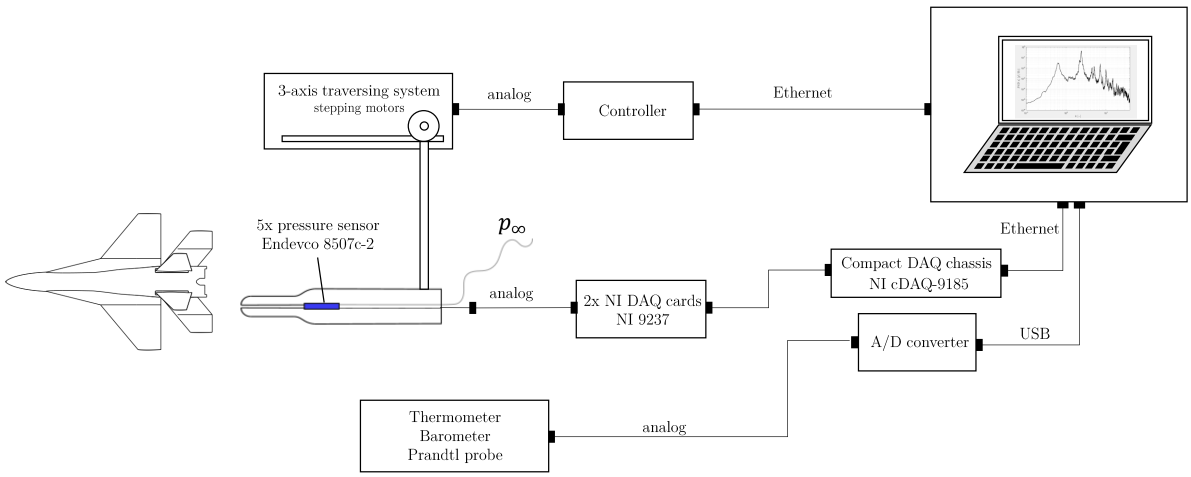

Figure 4: Measurement setup based on Heckmeier et al. [32]

DOI: 10.13009/EUCASS2023-297

2.4 Measurement conditions

Both the Stereo-PIV and the FRAP measurements were performed at the TUM-AER wind tunnel A, a Göttingen type wind tunnel. The dimensions of the open test section of the wind tunnel are 1.80 m in width and 2.40 m in height, with a length of 4.80 m. The maximum velocity achievable in the open test section is 65 m/s, and the turbulence intensity in each coordinate direction is kept below 0.4%. The measurement conditions can be found in Table 3. For the Stereo-PIV measurements, the Reynolds number related to the freestream velocity is set to $Re_{1/m} = 3.2 \times 10^6$ 1/m, which corresponds to a required freestream velocity of about $U_\infty = 51$ m/s and a Mach number of about $Ma_\infty = 0.15$. Due to the vibrations of the probe boom located in the flow, the Reynolds number had to be reduced to $Re_{1/m} = 2.0 \times 10^6$ 1/m for the FRAP measurements. This results in a freestream velocity of about $U_\infty = 32$ m/s and a Mach number of about $Ma_\infty = 0.09$. In both cases, fully turbulent boundary layers are present at all angles of attack to form the large-scale leading-edge vortices. Measurements are performed for an AoA of $\alpha = 25°$ and $\alpha = 35°$. The model blockage at the maximum possible AoA of $\alpha = 40°$ for the presented model setup is 5.6%.

Table 3: Wind tunnel measurement contitions

Parameter	**Value**
Mach number Ma_∞ - PIV/FRAP	0.15/0.09 [−]
Reynolds number $Re_{1/m} = (\rho_\infty U_\infty)/\mu$ - PIV/FRAP	$3.2 \times 10^6/2.0 \times 10^6$ [1/m]
Freestream velocity U_∞ - PIV/FRAP	51/32 [m/s]
Angle of attack α	25° and 35°

3. Results and discussion

3.1 Flow field

An overview of the basic flow physics of the delta wing design at low speeds will be given with the development of the non-dimensional axial vorticity $(\omega_x l_\mu)/U_\infty$ along the wing and the tails for $\alpha = 25°$ (left-hand side) and $\alpha = 35°$ (right-hand side) measured with Stereo-PIV, as shown in Fig. 5 for the rigid aluminum configuration. For both $\alpha = 25°$ and $\alpha = 35°$, it can be seen that two primary vortices form at the leading edges of the wing. As mentioned in subsection 2.2, the first plane near the apex of the wing could not be measured for $\alpha = 35°$ and is accordingly not shown. Already in the low AoA range, the pressure-induced flow around the highly swept leading edge can no longer follow the wing contour, resulting in flow separation. Under the impact of the externally entrained flow, the detached free shear layer rolls up, and a large-scale leading edge vortex forms. Once fully developed, the inboard strake vortex (IBV) extends up to the apex and rolls up along the leading edge of the strake (slender wing section), while the second primary vortex, also called the midboard vortex (MBV), is formed at the kink of the leading edge (non-slender wing section). The vortex core is characterized by high axial velocities, low static pressure, and lower total pressure due to high dissipation in the sub-core [1]. Low static pressure causes the IBV and the MBV to move towards each other, resulting in an interaction. As shown in Fig. 5, the vortices become unstable downstream from a certain point, leading to vortex bursting due to an adverse pressure gradient. Thereby, the vortex core expands rapidly, and high pressure fluctuations result [35]. The core flow upstream of breakdown is of jet-type and downstream of breakdown it is of wake-type. The transition from jet- to wake-type is characterized by rapid change in the axial velocity profiles [35]. With increasing AoA, the burst location moves upstream [1]. This can also be seen in the Stereo-PIV results in Fig. 5, where the IBV is still stable at $\alpha = 25°$ just before the kink but has already burst at $\alpha = 35°$. Both vortices have already burst in the tail area, resulting in a dynamic structural response (buffeting) of the HTP and fins [12].

3.2 Vortex trajectories and axial core velocities

In the following section, the vortex core trajectories and axial core velocities obtained from the Stereo-PIV measurements are discussed for $\alpha = 25°$ and $\alpha = 35°$ for the rigid and the flexible case. The vortex core trajectories and core flow characteristics are tracked by evaluating the Q-criterion for a jet-type vortex. The Q-criterion serves as a criterion for identifying vortex structures by defining a vortex as a contiguous fluid region where the second invariant of the velocity gradient is positive. These areas are characterized by having a higher magnitude of vortex strength compared

DOI: 10.13009/EUCASS2023-297

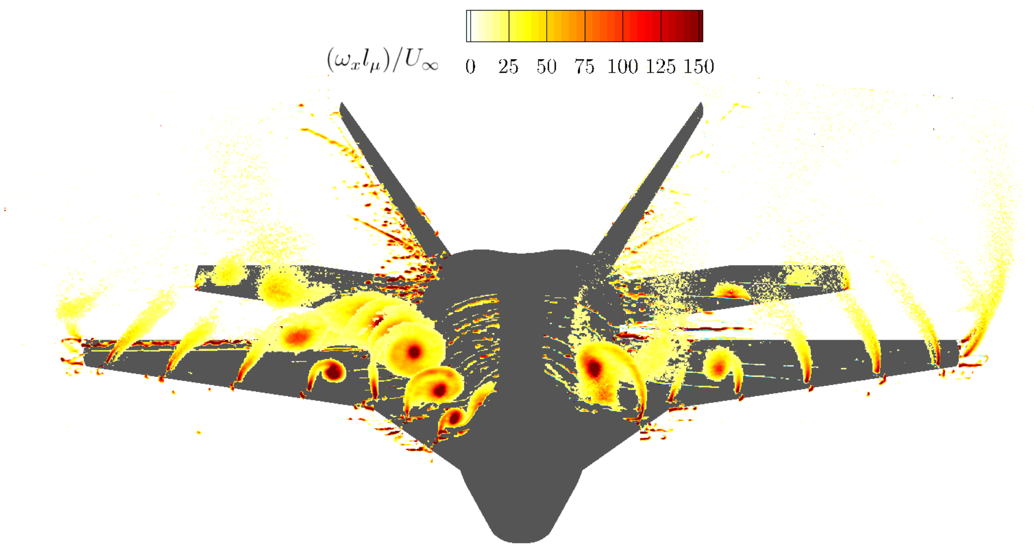

Figure 5: Non-dimensional axial vorticity $(\omega_x l_\mu)/U_\infty$ for $\alpha = 25°$ (left) and $\alpha = 35°$ (right) measured with Stereo-PIV

to the shear rate within these regions. The Q-criterion is calculated by [36]

$$Q = \frac{1}{2}\left(u_{i,i}^2 - u_{i,j}u_{j,i}\right) = -\frac{1}{2}u_{i,j}u_{j,i} = \frac{1}{2}\left(\|\Omega\|^2 - \|S\|^2\right) > 0 \tag{1}$$

with Ω defining the vorticity tensor and S the strain rate tensor. The maximum value of the Q-criterion indicates the jet-type vortex core. The position of the wake-type core is set to the minimum of the velocity magnitude inside an annular vorticity concentration. Thus, the trajectories can also be detected downstream of vortex breakdown.

Figure 6 shows the vortex trajectories and non-dimensional axial velocities u_x/U_∞ in the vortex core of IBV and MBV of the rigid and the flexible configuration for $\alpha = 25°$ (left-hand side) and $\alpha = 35°$ (right-hand side). In Fig. 6a and 6c, it can be seen that the spanwise and vertical trajectories of IBV and MBV are almost identical for the rigid and the flexible configuration for $\alpha = 25°$. In spanwise direction, the trajectories of IBV and MBV do not cross but move towards each other, especially for the last two trackable axial flow cross-sections in the downstream direction $x/c_{r,W} = 1.02$ and $x/c_{r,W} = 1.08$. In the vertical direction, the MBV moves upwards, while the IBV moves downwards towards the wing from $x/c_{r,W} = 0.94$. The vertical trajectories of IBV and MBV cross each other between $x/c_{r,W} = 0.94$ and $x/c_{r,W} = 1.02$. For $\alpha = 35°$, the spanwise trajectories of IBV and MBV in Fig. 6b are also almost identical for the rigid and the flexible case and can be tracked until $x/c_{r,W} = 0.94$. In contrast to $\alpha = 25°$, the vortices move away from each other in a spanwise direction. In Fig. 6d, it can be seen that the vertical trajectories of IBV and MBV meet at the last observable position. In the case of the IBV, slight differences can be seen at the first shown position at $x/c_{r,W} = 0.64$ between the two cases. The trajectory of the rigid case starts a little higher in the vertical direction.

Figures 6e and 6f show the non-dimensional axial velocities u_x/U_∞ in the vortex core. At $\alpha = 25°$, it can be seen that the axial core velocity of the IBV increases at first until $x/c_{r,W} = 0.79$ and then decreases slightly until $x/c_{r,W} = 0.94$ before dropping rapidly. The sudden sharp decrease in axial core velocity indicates the start of the breakdown process. Up to this point, the axial core velocities in the rigid case are higher than in the flexible case. The maximum deviation is at $x/c_{r,W} = 0.94$, where the axial core velocity of the flexible configurations is about 90% of the rigid configuration. In contrast, at the last trackable point $x/c_{r,W} = 1.08$ in the wake-type region, the axial core velocity is slightly higher for the flexible case, indicating slightly upstream vortex bursting for the rigid configuration. The maximum axial core velocities of the IBV are measured in the plane at $x/c_{r,W} = 0.79$ and are $u_x = 2.7U_\infty$ in the rigid case and $u_x = 2.45U_\infty$ in the flexible case. The maximum core velocities of the MBV are at the beginning of its development at $x/c_{r,W} = 0.86$ with $u_x = 1.86U_\infty$ for the rigid configuration and $u_x = 1.93U_\infty$ for the flexible configuration. Larger differences between the rigid and the flexible case are seen in the next two measurement planes after a sharp drop in core velocities. The largest difference can be observed at $x/c_{r,W} = 0.94$ with a 1.5 times higher axial core velocity for the flexible configuration. In the bursting area, the axial velocities of IBV and MBV converge.

At $\alpha = 35°$, the axial velocities of both the IBV and the MBV drop rapidly from the first position shown in Fig.6f. Thus, the maximum measured values for the IBV in the plane $x/c_{r,W} = 0.64$ are at $u_x = 2.44U_\infty$ for the rigid case and at $u_x = 2.42U_\infty$ for the flexible case. For the MBV, the values are maximum in the $x/c_{r,W} = 0.86$ plane with $u_x = 0.79U_\infty$ for the rigid configuration and $u_x = 0.77U_\infty$ for the flexible configuration. The significantly lower axial core velocities

DOI: 10.13009/EUCASS2023-297

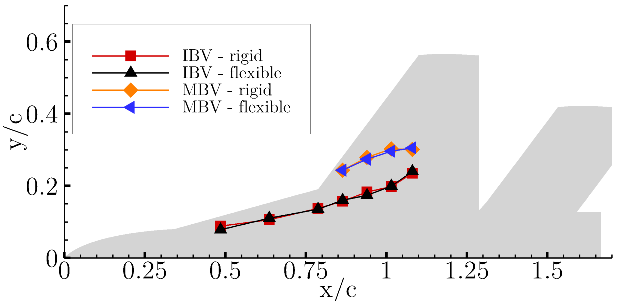

(a) Spanwise vortex trajectories for $\alpha = 25°$

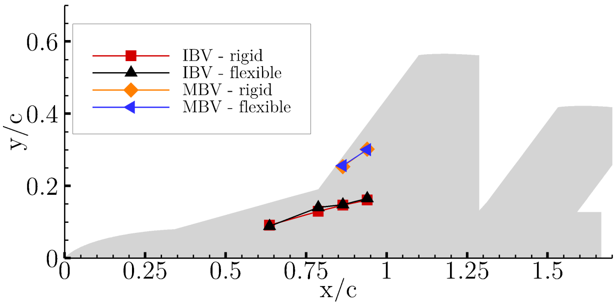

(b) Spanwise vortex trajectories for $\alpha = 35°$

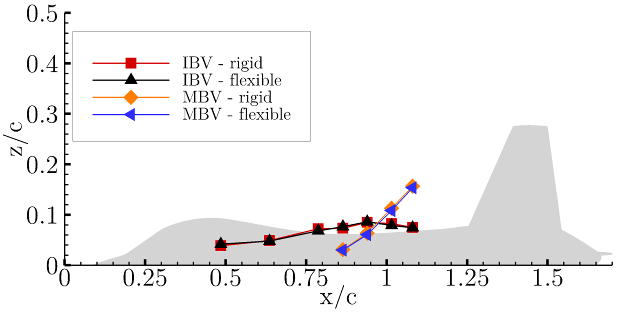

(c) Vertical vortex trajectories for $\alpha = 25°$

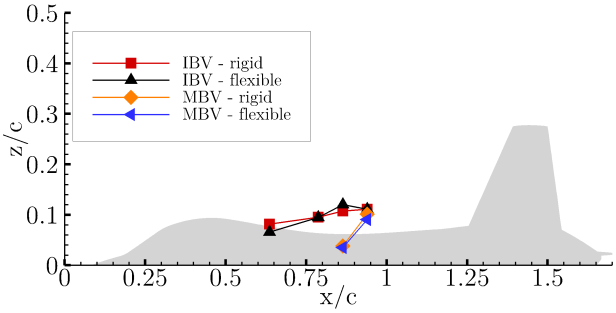

(d) Vertical vortex trajectories for $\alpha = 35°$

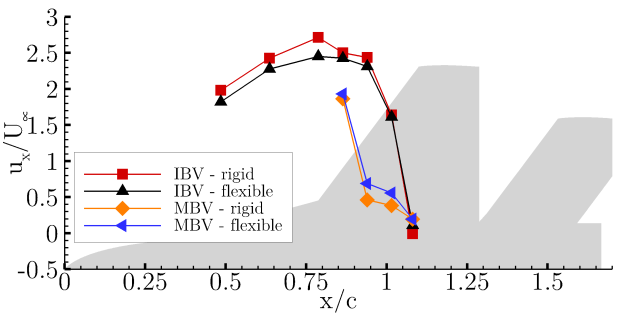

(e) u_x/U_∞ along the vortex core for $\alpha = 25°$

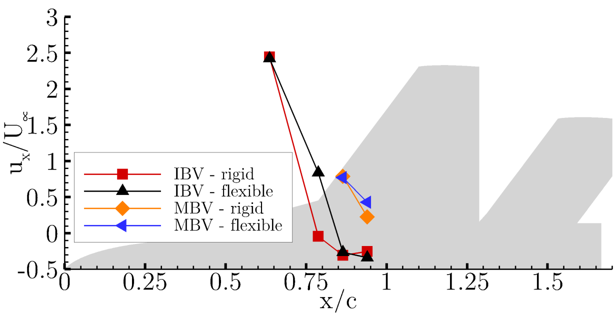

(f) u_x/U_∞ along the vortex core for $\alpha = 35°$

Figure 6: Vortex trajectories and non-dimensional axial velocities u_x/U_∞ in the vortex core of IBV and MBV of the rigid and the flexible configuration for $\alpha = 25°$ and $\alpha = 35°$

of the IBV of $u_x = -0.04U_\infty$ in the rigid case compared to $u_x = 0.84U_\infty$ in the flexible case at $x/c_{r,W} = 0.79$ indicate a clear upstream vortex bursting. For the MBV, the axial core velocity in the last trackable position at $x/c_{r,W} = 0.94$ is 1.9 times higher in the flexible case than in the rigid case. As with the IBV, this indicates a more upstream located vortex breakdown in the rigid configuration for the MBV as well. In contrast to $\alpha = 25°$, the axial velocities in the area of vortex bursting differ significantly between IBV and MBV.

In summary, there are no significant differences in the spanwise and vertical vortex trajectories between the rigid and the flexible configuration. At $\alpha = 25°$, the axial velocities between IBV and MBV converge in the burst region with previously higher IBV and lower MBV core velocities of the rigid configuration. At $\alpha = 35°$, the axial core velocities of IBV and MBV do not converge in the bursting region. A steeper drop in the axial core velocity curves in the rigid case indicates a clear upstream located bursting of IBV and MBV.

3.3 Flow field in the breakdown region

In the following section, the flow field in the breakdown area is analyzed and discussed in terms of the non-dimensional axial velocity u_x/U_∞ and the non-dimensional axial vorticity $(\omega_x l_\mu)/U_\infty$ based on the results of the Stereo-PIV measurements for $\alpha = 25°$ and $\alpha = 35°$. Figure 7 shows the flow field characteristics for the last two trackable vortex core trajectory points $x/c_{r,W} = 1.02$ and $x/c_{r,W} = 1.08$ (see Fig. 6) for $\alpha = 25°$ of the rigid (left-hand side) and the

DOI: 10.13009/EUCASS2023-297

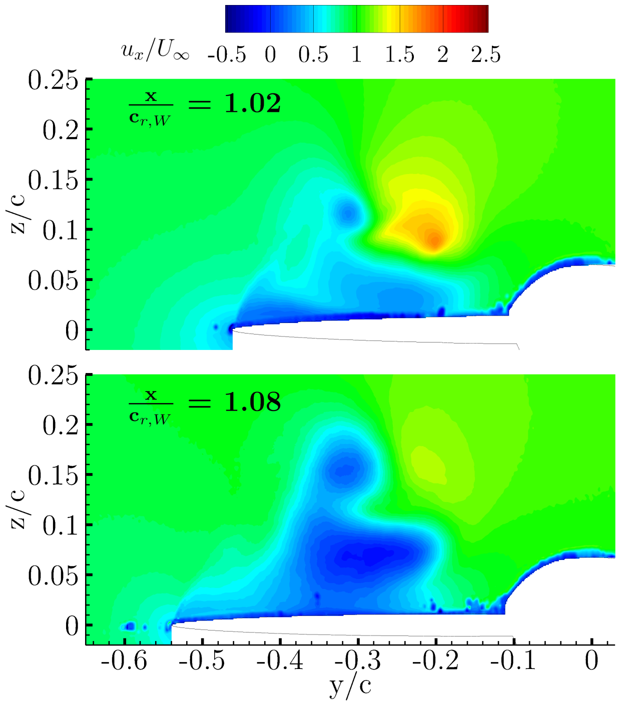

(a) u_x/U_∞ for the rigid configuration

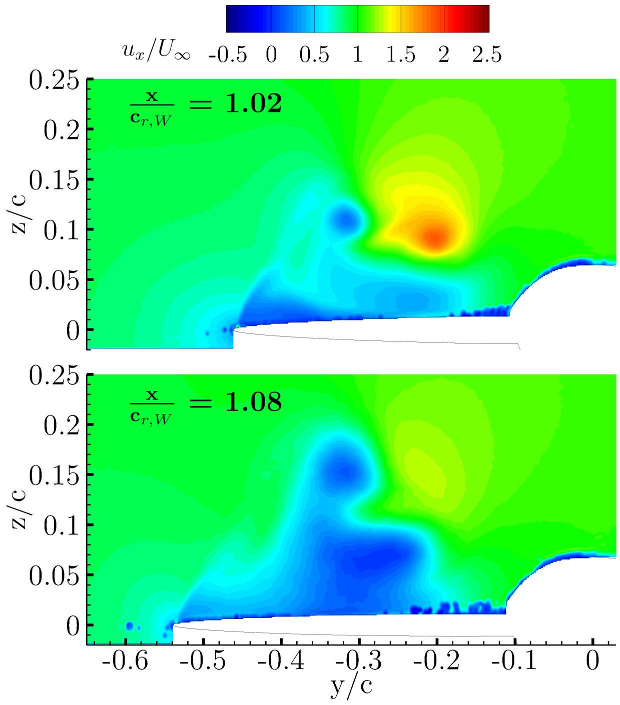

(b) u_x/U_∞ for the flexible configuration

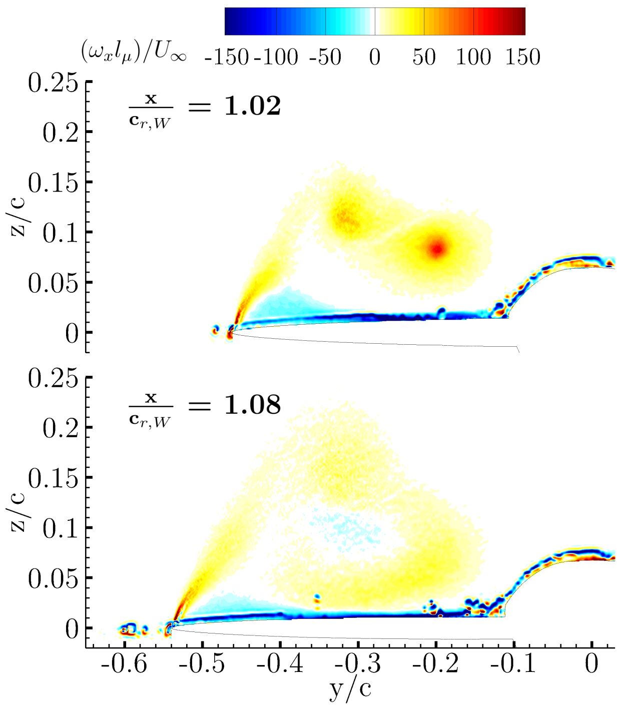

(c) $(\omega_x l_\mu)/U_\infty$ for the rigid configuration

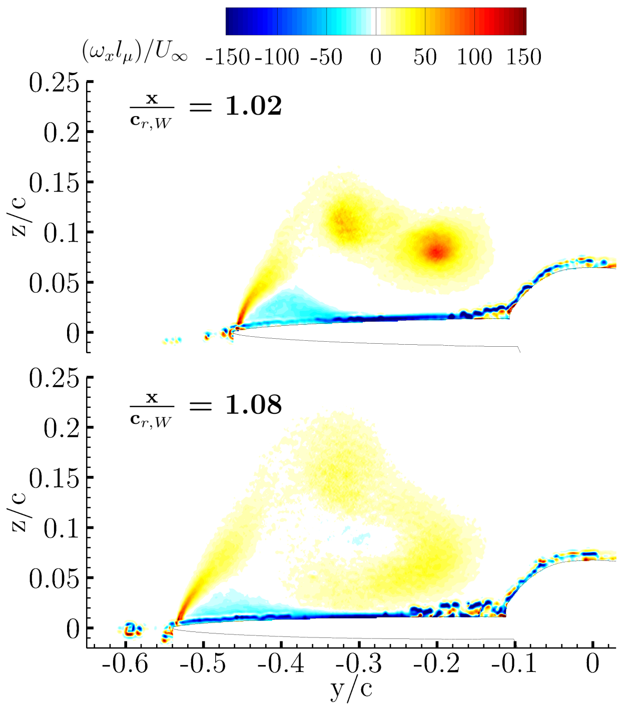

(d) $(\omega_x l_\mu)/U_\infty$ for the flexible configuration

Figure 7: u_x/U_∞ and $(\omega_x l_\mu)/U_\infty$ for $\alpha = 25°$ for the rigid and the flexible configuration

flexible (right-hand side) configuration. No major differences between the rigid and flexible configurations can be seen in both measurement planes. At $x/c_{r,W} = 1.02$, the IBV and MBV vortex structures are clearly visible. As it can also be seen in Fig. 6e, significantly higher axial core velocities are measured in this cross-flow section for the IBV than for the MBV. While the IBV is still stable, the MBV is already bursting. This can also be observed in the vorticity, which is still significantly higher in the core area of the IBV than in the MBV. A blue area with low axial velocity can be seen above the wing. This effect results from the vortex axis of the IBV pointing outwards towards the tip and

DOI: 10.13009/EUCASS2023-297

thus not being perpendicular to the measurement plane. Thus, the rotating flow creates an additional negative velocity component against the main flow perpendicular to the yz-plane. At $x/c_{r,W} = 1.08$, the vortex core velocities of IBV and MBV decrease to a low value, as it can also be seen in Fig. 6e. The IBV vertically moves under the MBV, while both vortices move horizontally towards each other. Comparing both measurement planes, a more abrupt transition from jet- to wake-type occurs for the IBV related to the slender section than for the MBV related to the non-slender section. This is consistent with the observations of Gursul et al. [37], whereby the vortex breakdown and the transition from jet-type to wake-type at high angles of attack exhibit less abrupt characteristics for non-slender wings, with the core expanding gradually and adopting a conical shape.
Figure 8 shows the flow field characteristics for the measurement planes at $x/c_{r,W} = 0.79$ just before the kink and $x/c_{r,W} = 0.86$ just after the kink for $\alpha = 35°$ of the rigid (left-hand side) and the flexible (right-hand side) configuration. In contrast to $\alpha = 25°$, apparent differences in the breakdown area between the two configurations can be identified. When considering the axial velocities, the blue area with $u_x/U_\infty < 1$ is significantly more prominent in the rigid case than in the flexible case, especially at $x/c_{r,W} = 0.79$. This can be explained by an earlier bursting of the IBV in the rigid case. While a small region of higher vorticity $(\omega_x l_\mu)/U_\infty$ can still be identified in the flexible configuration, the vortex core in the rigid configuration has already expanded significantly into an annular shape and exhibits lower vorticity. Gursul and Xi [38] observed in their water tunnel investigations with a slender delta wing at higher angles of attack between $\alpha = 25°$ and $\alpha = 35°$ that the breakdown location moves further upstream when there is a flat plate parallel to the freestream downstream of the breakdown location. Similar effects could explain the later bursting in the flexible case since the flexible tails respond to the unsteady pressure fluctuations and thus intervene more weakly with the flow. To study the possible influence of the wing's flexibility on the vortex breakdown position, further investigations have to be made with mixed configurations (flexible wing with rigid tails and rigid wing with flexible tails).
In the measurement plane $x/c_{r,W} = 0.86$, shortly after the kink, the MBV is formed, while the IBV has already burst. Thus, in contrast to $\alpha = 25°$, a lower interaction of the vortices occurs, which is also visible in Fig. 6b due to the non-approximating trajectories and axial core velocities. The more extensive area of low axial velocities u_x/U_∞ and low vorticity $(\omega_x l_\mu)/U_\infty$ within the annular structure illustrates the more advanced stage of vortex bursting in the rigid configuration.
In summary, at $\alpha = 25°$, there are hardly any differences in the vortex flow between the flexible and the rigid configurations for the measurement planes considered around the bursting area. At $\alpha = 35°$, a significantly more upstream located vortex breakdown of the IBV in the rigid configuration is evident, leading to potentially enhanced downstream excitation (buffet) of aircraft structures due to the resulting pressure fluctuations.

3.4 Spectral analysis of the flow field

The pressure fluctuations responsible for the aerodynamic excitation (buffet) and the potentially associated dynamic structural response (buffeting) are analyzed in the following using the power spectral density (PSD) of the pressure fluctuation c_p' of the FRAP-measurement results. In the course of this, by using the non-dimensional turbulent kinetic energy (TKE) distribution from the Stereo-PIV measurements, three selected points are analyzed in one plane at $x/c_{r,W} = 1.02$ over the wing and two planes at $x/c_{r,W} = 1.37$ and $x/c_{r,W} = 1.54$ in the tail area for $\alpha = 25°$. For this AoA, the dynamic structural response is maximum according to [12]. For the spectral analysis, only the central sensor of the FRAP in the main flow direction is considered.
The non-dimensional TKE is calculated with [39]:

$$\mathrm{TKE} = \frac{u_{\mathrm{rms}}^2 + v_{\mathrm{rms}}^2 + w_{\mathrm{rms}}^2}{2U_\infty^2} \tag{2}$$

Figure 9 shows the TKE distribution at $x/c_{r,W} = 1.02$ over the wing with a stable IBV and a MBV at the beginning of the breakdown (see Fig. 7). The shear layer of the MBV is still well visible. Observing the energy spectra of the field pressure fluctuations of the rigid and the flexible case, a peak between $k = 2$ and $k = 4$ can be seen at all three positions with maxima between $k = 2.96$ and $k = 3.24$. This corresponds to the investigations of Breitsamter [35], in which immediately after bursting, a concentration of turbulent kinetic energy occurs in a still relatively broadband range between $k = 2$ and $k = 4$. This buffet peak is supposed to be associated with the helical mode instability (HMI) of the MBV. Due to the invasive measurement method, FRAP measurements in the IBV area were not possible because of the lack of accessibility due to the position of the tails. At the upper right position ($PSD\ c_p'$ on the right-hand side of Fig. 9), the peak is lower in the flexible case than in the rigid case. This can be explained by the FRAP measurement position relative to the TKE distribution, which is closer to the region of concentrated turbulent kinetic energy in the rigid configuration. A second smaller peak between $k = 1$ and $k = 2$ is identifiable, especially at the outer two positions related to the bursting MBV (marked with a square and triangle), where the shear layer is still clearly visible. Therefore, the peak is probably due to a shear layer instability (SLI). Its frequency range agrees with the investigations of Sedlacek

DOI: 10.13009/EUCASS2023-297

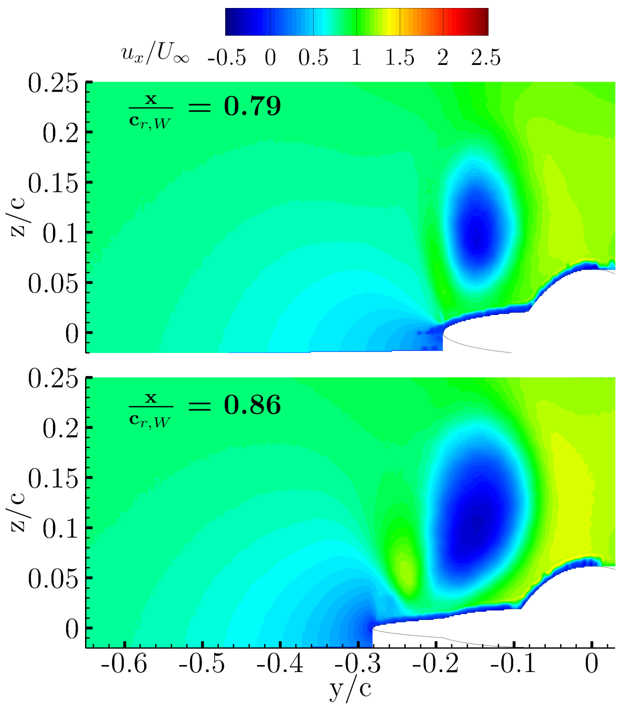

(a) u_x/U_∞ for the rigid configuration

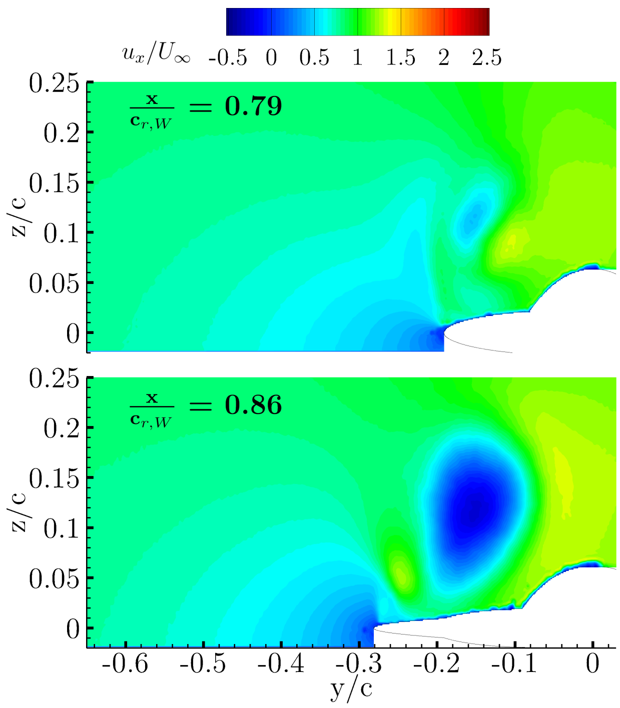

(b) u_x/U_∞ for the flexible configuration

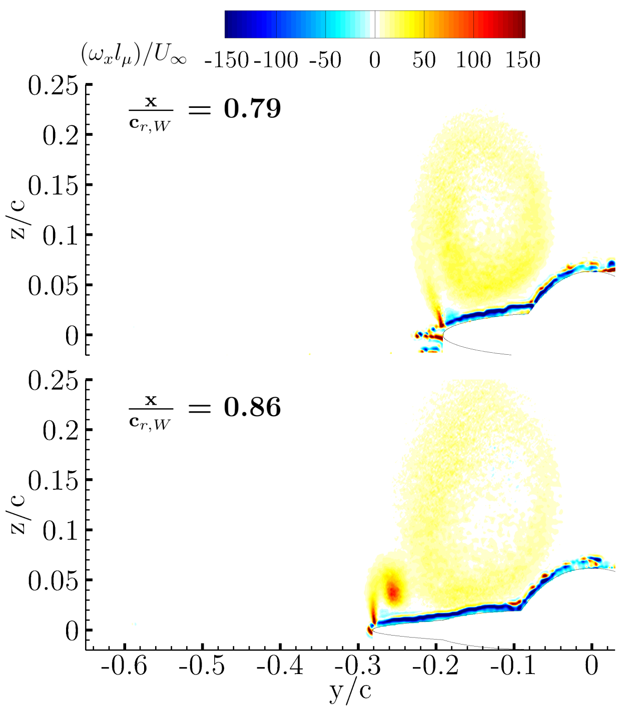

(c) $(\omega_x l_\mu)/U_\infty$ for the rigid configuration

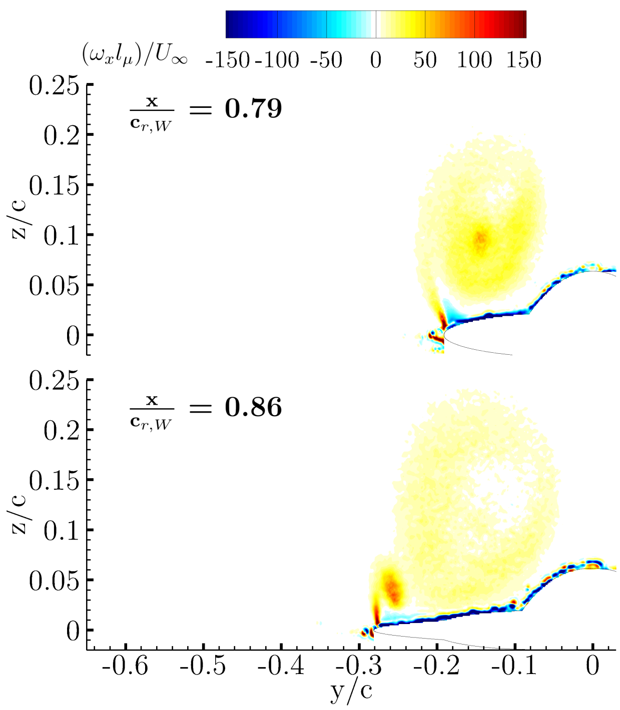

(d) $(\omega_x l_\mu)/U_\infty$ for the flexible configuration

Figure 8: u_x/U_∞ and $(\omega_x l_\mu)/U_\infty$ for $\alpha = 35°$ for the rigid and the flexible configuration

et al. [21], where a pronounced peak at $k \approx 1.88$ for $\alpha = 24°$ for a triple-delta configuration probably occurs due to the SLI.

Figure 10 shows in the TKE distributions that IBV and MBV have already burst in the measurement plane $x/c_{r,W} = 1.37$ between fin and HTP. In the PSD of the pressure fluctuations, a narrow-band peak in the range between $k = 1.22$ and $k = 1.28$ can be identified at all three measurement points for both configurations. The narrow-band concentration of field pressure fluctuations occurs in this frequency range presumably due to HMI. With increasing distance downstream

DOI: 10.13009/EUCASS2023-297

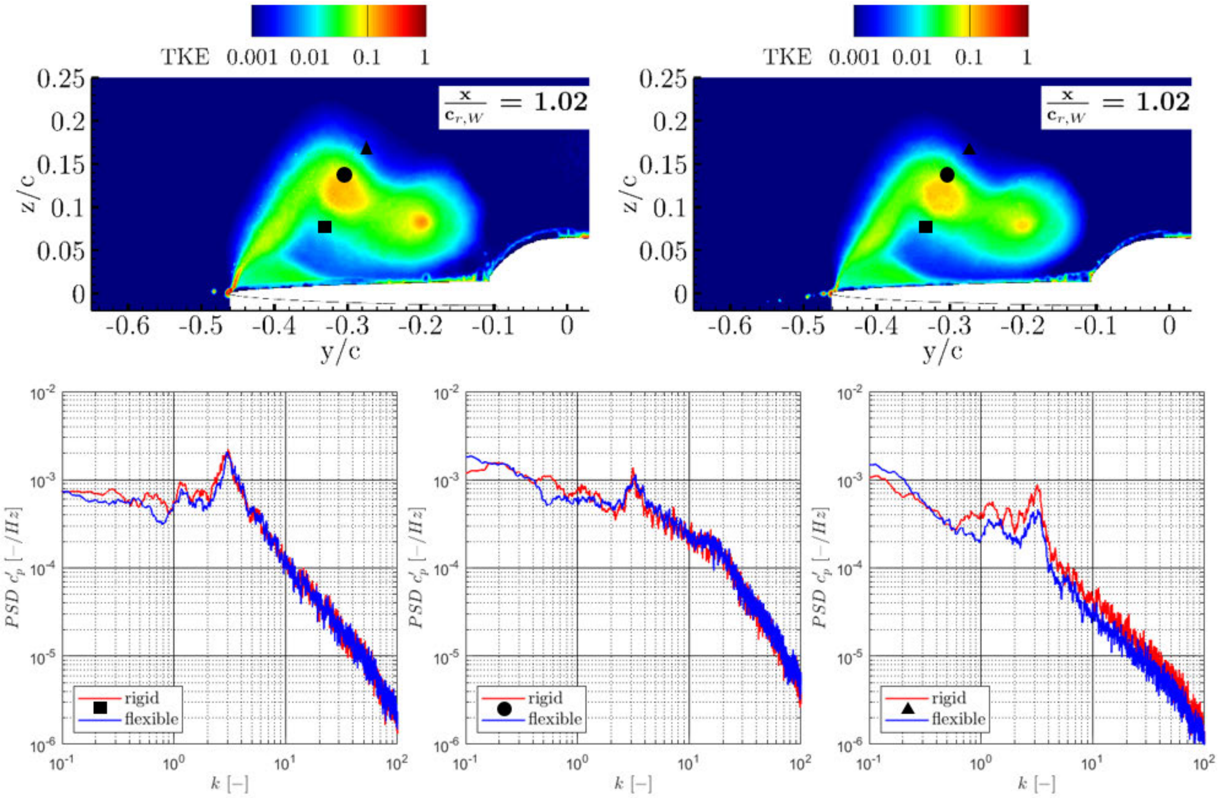

Figure 9: TKE for the rigid (left) and the flexible (right) configuration and PSD c_p' at $x/c_{r,W} = 1.02$

after the onset of the bursting process, the frequency band of increased concentration of TKE decreases and shifts to smaller k [35]. When comparing the PSD of the pressure fluctuations between the two measurement planes downstream of the vortex burst, a shift of the buffet peak to smaller reduced frequencies and a narrow band concentration is seen in the present investigations. However, it must be considered in the frequency analysis that at the measurement plane $x/c_{r,W} = 1.02$ the IBV is still stable, while the MBV is in the breakdown process and is mainly responsible for the formation of the buffet peak, whereas at $x/c_{r,W} = 1.37$ both vortices have already interacted and burst. Calculating the frequency range k_H of the HMI analytically by [1, 21]

$$\varphi_{m,\mathrm{eff}} = \arccos\left(\frac{F_1\cos\varphi_{W,1} + F_2\cos\varphi_{W,2}}{F_1 + F_2}\right) = 59.74^\circ \quad \text{with } F_1 = 1 \text{ and } F_2 = 2 \tag{3}$$

$$k_H = \frac{1}{\cot(\varphi_{m,\mathrm{eff}})\cdot\sin(\alpha)}\cdot(0.28 \pm 0.025) = [1.03; 1.24] \tag{4}$$

it can be observed that the measured peaks between $k = 1.22$ and $k = 1.28$ and the analytical solution of the HMI fit very well for the HTP and fin area for $\alpha = 25^\circ$. The HMI is associated with the dominant frequencies of the aerodynamic excitation (Buffet) [1]. When comparing the two configurations, at the top of the three measurement points (marked as a triangle), the buffet peak in the flexible case has significantly less energy content. This is consistent with the TKE distributions showing higher values (yellow areas) in the rigid case around this measurement point. The buffet peak is also weaker for the flexible configuration in the left bottom point (marked as a square).

PSD curves and Buffet peak frequencies similar to those at $x/c_{r,W} = 1.37$ are observed in the plane $x/c_{r,W} = 1.54$ in Fig.11 between $k = 1.24$ and $k = 1.30$ at the far end of the fin with a higher energy content of the buffet peak at the left bottom point (marked as a square). The TKE distribution in this measurement plane is additionally influenced by the formation of a stable vortex at the non-slender HTP ($\varphi_{HTP} = 40^\circ$). In the case of a stable vortex, high values of TKE are found in the vortex core, however, without noticeable amplitude increase in the energy spectra [35]. Although the vortex has a global influence on the burst region of IBV and MBV and shifts it upward, it is not supposed to significantly influence the frequency content of the peaks in the PSD of the pressure fluctuations. In the rigid configuration, the yellow area with high TKE in the upper region of the Stereo-PIV measurement plane is broader than in the flexible case. It affects the spectra of the upper measurement point (marked as a triangle). The buffet peak is consequently slightly higher in the rigid case.

DOI: 10.13009/EUCASS2023-297

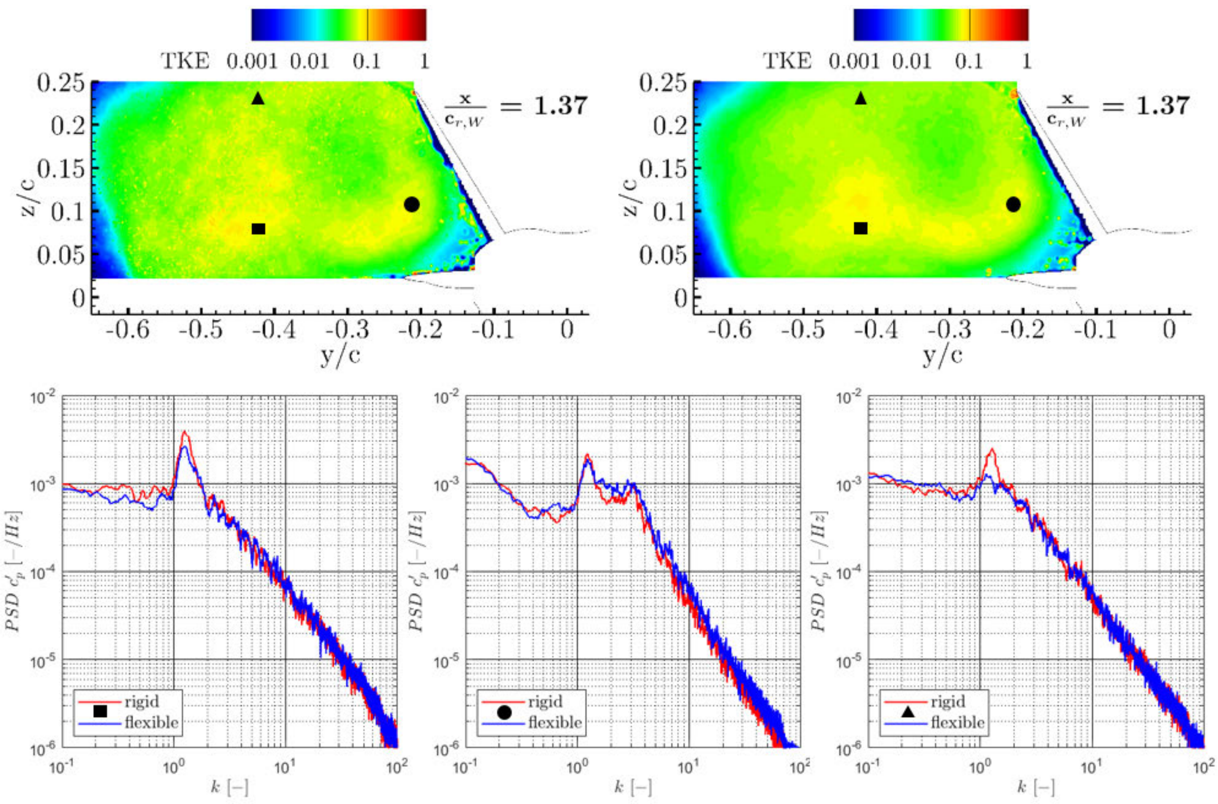

Figure 10: TKE for the rigid (left) and the flexible (right) configuration and PSD c_p' at $x/c_{r,W} = 1.37$

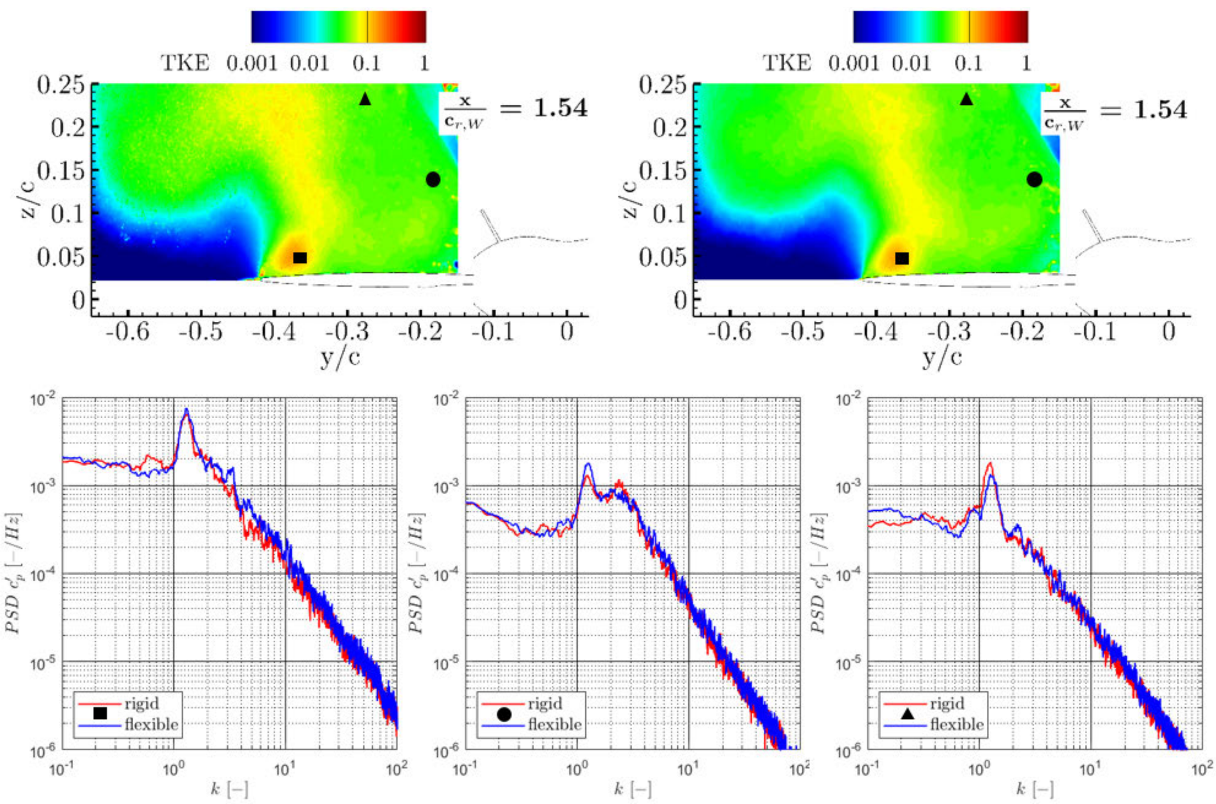

Figure 11: TKE for the rigid (left) and the flexible (right) configuration and PSD c_p' at $x/c_{r,W} = 1.54$

DOI: 10.13009/EUCASS2023-297

In summary, the aerodynamic excitation responsible for the dynamic structural response can be observed in all three measurement planes in the form of field pressure fluctuations concentrated in a specific frequency band (buffet peak). Due to minor differences in vortex position and burst flow field, there are slight differences in the magnitude of the buffet amplitudes, with a tendency to higher values for the rigid configuration.

4. Conclusion

In this study, stereoscopic particle image velocimetry (Stereo-PIV) measurements for the analysis of the flow field over a modular full-span wind tunnel model with either rigid or flexible wings and tail planes for tail buffeting analysis are performed at the low-speed TUM-AER wind tunnel A for $\alpha = 25°$ and $\alpha = 35°$. The double-delta wings with a sweep angle of $\varphi_{W,1} = 76°$ at the strake and $\varphi_{W,1} = 40°$ at the outboard wing section act as vortex generators. High pressure fluctuations downstream of the burst vortices are responsible for the potential aerodynamic excitation (buffet) of the tails and the associated dynamic structural response (buffeting). When comparing the rigid reference configuration with the flexible configuration, no significant differences can be seen in the spanwise and vertical vortex trajectories. While for $\alpha = 25°$ the axial core velocities u_x/U_∞ are lower in the flexible case until vortex breakdown, the steeper drop in axial core velocities for $\alpha = 25°$ and $\alpha = 35°$ indicates earlier bursting for the rigid configuration. When considering the axial velocity and vorticity distributions in the measurement planes for the area of vortex bursting, a significantly more upstream located vortex breakdown of the inboard strake vortex in the rigid configuration is present for $\alpha = 35°$. To analyze the narrow-band concentration of turbulent kinetic energy responsible for tail buffeting, the power spectral densities of the pressure fluctuations in terms of c'_p, measured with a fast-response aerodynamic pressure probe, are considered for $\alpha = 25°$ at selected points in three measured cross-flow planes along with the turbulent kinetic energy distributions from the Stereo-PIV measurements. Due to the helical mode instability, the buffet peaks occur in the measured cross-flow plane above the wing at $x/c_{r,W} = 1.02$ at a reduced frequency between $k = 2.96$ and $k = 3.24$ and in the tail area at $x/c_{r,W} = 1.37$ and $x/c_{r,W} = 1.54$ in a range between $k = 1.22$ and $k = 1.30$. While the buffet frequencies are very similar between the rigid and the flexible configurations, the magnitude of the buffet amplitudes differs with a tendency to higher values for the rigid configuration.
For a deeper understanding of the influence of the flexible components on the vortex topology and on the bursting behavior, further investigations have to be performed. Stereo-PIV measurements with mixed configurations (rigid wings with flexible tails and flexible wings with rigid tails) will be made to study the upstream and downstream effects of flexible components on the flow field. For analyzing the unsteady pressures on the surfaces of the wing and the tails as well as the dynamic three-dimensional structural deformation with a high spatial and temporal resolution, optical measurements with fast-response pressure sensitive paint (iPSP) and optical deformation measurements will be performed simultaneously.

5. Acknowledgments

The project is funded by the Deutsche Forschungsgemeinschaft (DFG, German Research Foundation) grant number BR 1511/15-1.

References

[1] Breitsamter, C.: Unsteady flow phenomena associated with leading-edge vortices. Progress in Aerospace Sciences **44**(1), 48–65 (2008). https://doi.org/10.1016/j.paerosci.2007.10.002

[2] Hirschel, E.H., Rizzi, A., Breitsamter, C., Staudacher, W.: Separated and Vortical Flow in Aircraft Wing Aerodynamics. Springer, Berlin (2021). https://doi.org/10.1007/978-3-662-61328-3

[3] Mabey, D.G.: Some Aspects of Aircraft Dynamic Loads Due to Flow Separation. Report, Advisory Group for Aerospace Research and Development (AGARD) (1988). https://doi.org/10.1016/0376-0421(89)90006-7

[4] John, H.: Critical Review of Methods to Predict the Buffet Capability of Aircraft. Report, Advisory Group for Aerospace Research and Development (AGARD) (1974)

[5] Rainey, G.A., Igoe, W.B.: Measurements of the Buffeting Loads on the Wing and Horizontal Tail of a 1/4-Scale Model of the X-1E Airplane. In: Field, L. (ed.) NACA Research Memorandum, vol. RM L58F25 (1958)

DOI: 10.13009/EUCASS2023-297

[6] Butoescu, V.A.J.: Similitude Criteria for Aeroelastic Models. INCAS BULLETIN **7**(Issue 1/ 2015), 37–50 (2015). https://doi.org/10.13111/2066-8201.2015.7.1.4

[7] Davis Jr., D.D., Huston, W.B.: The Use of Wind Tunnels to Predict Flight Buffet Loads. Report NACA Research Memorandum RM L57D25, NACA (1957)

[8] Hanson, P.W.: Evaluation of an aeroelastic model technique for predicting airplane buffet loads. Report, NASA Langley Research Center (1973)

[9] Zan, S., Huang, X.Z.: Wing and FIN Buffet on the Standard Dynamics Model. Report Verification and Validation Data for Computational Unsteady Aerodynamics ADP010722, Defense Technical Information Center (2001)

[10] Katzenmeier, L., Vidy, C., Kolb, A., Breitsamter, C.: Aeroelastic wind tunnel model for tail buffeting analysis using rapid prototyping technologies. CEAS Aeronautical Journal **12**, 633–651 (2021). https://doi.org/10.1007/s13272-021-00523-9

[11] Stegmüller, J., Katzenmeier, L., Breitsamter, C.: Horizontal tail buffeting characteristics at wing vortex flow impact. CEAS Aeronautical Journal **13**, 779–796 (2022). https://doi.org/10.1007/s13272-022-00593-3

[12] Stegmüller, J., Hayböck, S., Hartl, P., Breitsamter, C.: Experimental Investigations of an Aeroelastic Wind Tunnel Model for Tail Buffeting Analysis. In: Congress of the International Council of the Aeronautical Sciences (ICAS) 2022, Stockholm, Sweden (2022)

[13] Verhaagen, N.G., Jenkins, L.N., Kern, S.B., Washburn, A.E.: A Study of the Vortex Flow over 76/40-deg Double-Delta Wing. Technical report, NASA Langley Research Center, Hampton, Virginia (1995)

[14] Cunningham Jr., A.M., den Boer, R.G., Dogger, C.S., Geurts, E.G.M., Persoon, A.J., Retel, A.P., Zwaan, R.J.: Unsteady Low-Speed Windtunnel Test of a Straked Delta Wing, Oscillating in Pitch. Technical report, National Aerospace Laboratory (NLR), Amsterdam, Netherlands (1988)

[15] Gonzalez, H.A., E., E.G., G., M.B., H., B.J.: Effects of Various Fillet Shapes on a 76/40 Double Delta Wing from Mach 0.18 to 0.7. In: RTO Applied Vehicle Technology Panel (AVT Symposium), vol. MP-069(I). Loen, pp. 48–14839 (2001)

[16] Woodiga, S.A., Liu, T.: Skin friction fields on delta wings. Experiments in Fluids **47**(6), 897–911 (2009). https://doi.org/10.1007/s00348-009-0686-6

[17] Brennenstuhl, U., Hummel, D.: Vortex Formation Over Double-Delta Wings. In: Congress of the International Council of the Aeronautical Sciences (ICAS) 1982, Seattle, Washington, pp. 1133–1146 (1982)

[18] Taylor, G.S., Gursul, I.: Buffeting flows over a low-sweep delta wing. AIAA Journal **42**(9), 1737–1745 (2004). https://doi.org/10.2514/1.5391

[19] Pfnür, S., Breitsamter, C.: Leading-edge vortex interactions at a generic multiple swept-wing aircraft configuration. Journal of Aircraft **56**(6), 2093–2107 (2019). https://doi.org/10.2514/1.C035491

[20] Sedlacek, D., Breitsamter, C.: Aerodynamic characteristics and topology of interfering vortex systems at hybrid-delta wings. Journal of Aircraft **60**(2), 331–347 (2023). https://doi.org/10.2514/1.C036947

[21] Sedlacek, D., Heckmeier, F., Usbek, A., Breitsamter, .: Analysis of vortex burst phenomena on generic hybrid delta wing planforms at subsonic speeds. In: Dillmann, A., Heller, G., Krämer, E., Wagner, C. (eds.) New Results in Numerical and Experimental Fluid Mechanics XIII, pp. 282–291. Springer, Cham (2021). https://doi.org/10.1007/978-3-030-79561-0_27

[22] Woppowa, S., Grosche, F.-R.: In: Körner, H., Hilbig, R. (eds.) Wind Tunnel and Water Tunnel Studies of Vertical Fin Buffeting, pp. 405–412. Vieweg+Teubner Verlag, Wiesbaden (1997). https://doi.org/10.1007/978-3-322-86573-1_51

[23] Wolfe, S., Lin, J.-C., Rockwell, D.: Buffeting at the leading-edge of a flat plate due to a streamwise vortex: Flow structure and surface pressure loading. Journal of Fluids and Structures **9**(4), 359–370 (1995). https://doi.org/10.1006/jfls.1995.1020

[24] Mayori, A., Rockwell, D.: Interaction of a streamwise vortex with a thin plate - a source of turbulent buffeting. AIAA Journal **32**(10), 2022–2029 (1994). https://doi.org/10.2514/3.12247

DOI: 10.13009/EUCASS2023-297

[25] Canbazoglu, S., Lin, J.-C., Wolfe, S., Rockwell, D.: Buffeting of fin - distortion of incident vortex. AIAA Journal **33**(11), 2144–2150 (1995). https://doi.org/10.2514/3.12959

[26] Canbazoglu, S., Lin, J.-C., Wolfe, S., Rockwell, D.: Buffeting of a fin - streamwise evolution of flow structure. Journal of Aircraft **33**(1), 185–190 (1996). https://doi.org/10.2514/3.46920

[27] Kim, Y., Rockwell, D., Liakopoulos, A.: Vortex buffeting of aircraft tail: Interpretation via proper orthogonal decomposition. AIAA Journal **43**(3), 550–559 (2005). https://doi.org/10.2514/1.9989

[28] Helmut, J.: Critical Review of Methods to Predict the Buffet Capability of Aircraft. Technical Report AGARD Report No. 623, Messerschmitt-Bölkow-Blohm GmbH, Munich, Germany (1974)

[29] Huang, X.Z.: Wing and Fin Buffet on the Standard Dynamics Model. Technical report, Field Technology Inc, Long Beach, CA (2000)

[30] Hinsch, K.D.: Three-dimensional particle velocimetry. Measurement Science and Technology **6**(6), 742 (1995). https://doi.org/10.1088/0957-0233/6/6/012

[31] Sciacchitano, A., Wieneke, B.: Piv uncertainty propagation. Measurement Science and Technology **27**(8), 084006 (2016). https://doi.org/10.1088/0957-0233/27/8/084006

[32] Heckmeier, F., Hayböck, S., Breitsamter, C.: Spatial and temporal resolution of a fast-response aerodynamic pressure probe in grid-generated turbulence. Experiments in Fluids **62**(44) (2021). https://doi.org/10.1007/s00348-021-03141-7

[33] Heckmeier, F., Breitsamter, C.: Aerodynamic probe calibration using gaussian process regression. Measurement Science and Technology **31**(12), 125301 (2020). https://doi.org/10.1088/1361-6501/aba37d

[34] Heckmeier, F., Iglesias, D., Kreft, S., Kienitz, S., Breitsamter, C.: Development of unsteady multi-hole pressure probes based on fiber-optic pressure sensors. Engineering Research Express **1**(2), 025023 (2019). https://doi.org/10.1088/2631-8695/ab4f0d

[35] Breitsamter, C.: Turbulente Strömungsstrukturen an Flugzeugkonfigurationen Mit Vorderkantenwirbeln. Doctoral Dissertation, Technical University of Munich, Munich (1997)

[36] Kolář, V.: Vortex identification: New requirements and limitations. International Journal of Heat and Fluid Flow **28**(4), 638–652 (2007). https://doi.org/10.1016/j.ijheatfluidflow.2007.03.004. Including Special Issue of Conference on Modelling Fluid Flow (CMFFâ06), Budapest

[37] Gursul, I., Gordnier, R., Visbal, M.: Unsteady aerodynamics of nonslender delta wings. Progress in Aerospace Sciences - PROG AEROSP SCI **41**, 515–557 (2005). https://doi.org/10.1016/j.paerosci.2005.09.002

[38] Gursul, I., Xie, W.: Buffeting flows over delta wings. Aiaa Journal - AIAA J **37**, 58–65 (1999). https://doi.org/10.2514/2.664

[39] Hövelmann, A.: Analysis and control of partly-developed leading-edge vortices. PhD thesis, Technical University of Munich (2016)